Sol-Enhanced Electrodeposition of Ni-Co-CeO_2 Nanocomposite Electrodes for Enhanced Electrochemical Performance in an Alkaline Media

Shayan Sarraf[1,a], Seyedeh Marzieh Hosseini[2,a], Saeed Rastegari[3,a,*], Mansour Soltanieh[4,a],

a School of Metallurgy and Materials Engineering, Iran University of Science and Technology, Narmak, Tehran 1684613114, Iran

1 Shayanhsarraf@gmail.com

2 mzh.hosseini@gmail.com

3 Rastegari@iust.ac.ir

4 Mansour_soltanieh@iust.ac.ir

* Corresponding Author

Abstract

In this study, Ni-Co-CeO_2 nanocomposite coatings were deposited on copper substrates via a sol-enhanced electrodeposition method. Cerium oxide nanoparticles were synthesized using cerium chloride precursor and HMTA as a precipitating agent at 70 °C and subsequently added to a Watts bath containing nickel and cobalt ions. An investigation of the effect of deposition current density (10 to 30 $mA.cm^{-2}$) revealed that increasing the deposition current density reduced the cerium oxide content in the coating from 12.2 to 7.1 wt%. SEM images confirmed a morphological transformation from an acicular structure to a fine-grained microstructure with surface heterogeneity in the presence of the nanoparticles. XRD results further demonstrated grain refinement induced by the CeO_2 reinforcing phase. Electrochemical evaluations in 1 M KOH solution showed that the sample deposited at a current density of 20 $mA.cm^{-2}$ exhibited the highest performance, with a discharge time of 92 seconds (a 77% improvement compared to the particle-free sample) and optimal charge transfer resistance. This enhanced performance is attributed to a favorable balance between the electrical conductivity of the metallic matrix and the catalytic activity of the cerium oxide nanoparticles. The findings of this investigation substantiate the efficacy of the sol-enhanced method in designing advanced electrodes for energy systems.

Keywords: Ni-Co-CeO_2 coatings, sol-enhanced electrodeposition, CV, EIS, GCD

1. Introduction

The development of high-performance energy storage and conversion systems has become a central focus of scientific research, driven by the growing demand for clean and renewable energy sources [1-3]. In this context, the design of electrodes exhibiting high catalytic activity and adequate stability in corrosive environments, particularly in alkaline solutions, plays a decisive role in improving the performance of such systems [4-6]. Despite the considerable potential of metallic materials, challenges such as limited electrochemically active surface area (ECSA) and high polarization hinder the achievement of optimal charge transfer rates [7-9]. Consequently, novel approaches based on surface engineering and the construction of nanocomposite structures have been pursued, aiming to exploit synergistic effects between metallic phases and oxide particles to effectively enhancing catalytic stability and charge storage capacity [10-12].

Among transition metals, bimetallic nickel-cobalt alloys have gathered considerable attention for electrocatalytic applications due to the synergistic effects between these two elements and their ability to undergo multiple redox reactions [13-15]. Compared with single-metal electrodes, these alloy systems offer higher current densities and superior mechanical stability over prolonged cycling, owing to their favorable electrical conductivity and overlapping chemical potentials [16-18]. Nevertheless, achieving an optimal crystalline structure that facilitates the diffusion of electrolyte ions remains a technical challenge [19-20].

The incorporation of secondary phases into metallic matrices can substantially enhance the electrochemical properties of metallic structures [21-23]. Among such phases, cerium oxide nanoparticles, owing to the distinctive structural and electronic characteristics of this metal oxide, represent a highly promising approach for the engineering of catalytic surfaces [24, 25]. Cerium oxide, an n-type semiconductor with high oxygen storage capacity (OSC), possesses Ce^{4+}/Ce^{3+} redox couples that enable it to function as an active co-catalyst [26, 27]. The presence of these particles during the co-deposition process not only leads to grain refinement and an increased electrochemically active surface area through heterogeneous nucleation mechanisms but also reduces the energy barrier of intermediate reactions by modifying the chemical environment surrounding nickel and cobalt atoms [28, 29]. By providing active oxygenated species at the electrode surface, these particles facilitate charge transfer kinetics and induce the resolution and improved definition of oxidation peaks in alkaline media [30]. Thus, the

[DOI: 10.22068/ijmse.4640]

integration of CeO_2 into a Ni-Co structure can establish an intelligent balance between the electrical conductivity of the metal and the chemical activity of the oxide [31].

One of the fundamental challenges in the fabrication of nanocomposite coatings via electrochemical methods is the limited stability of particles within the electrolyte and their pronounced tendency to agglomerate, which can lead to incomplete co-deposition and, consequently, deterioration of the final coating properties [32, 33]. To overcome this limitation, the sol-enhanced electrodeposition technique has been reported as an effective approach for incorporating secondary-phase particles into metallic matrices [34, 35]. In this methodology, the secondary phase is prepared as a stable colloidal suspension (sol) rather than being introduced as dry powder and is subsequently added to the plating bath [36, 37]. The selection of a suitable precipitating agent that is compatible with the electrodeposition electrolyte is a key factor in the successful application of this method [38]. Compared with conventional particle co-deposition, the sol-enhanced approach reduces particle agglomeration and promote a more uniform distribution and incorporation of the secondary phase within the metallic matrix. This feature provides a suitable platform for obtaining controlled microstructures and specific morphologies tailored for electrochemical energy-related applications [39, 40].

Considering the aforementioned advantages, the primary objective of the present study is the development and electrochemical evaluation of Ni-Co-CeO_2 nanocomposite coatings using a sol-enhanced electrodeposition method. In this investigation, particular emphasis is placed on the role of deposition current density as a key parameter governing the oxide particle content, microstructure, and surface morphology. Subsequently, the physical and structural characteristics of the nanoparticles and the resulting coatings are examined, followed by an analysis of their electrochemical behavior in terms of charge storage capacity and catalytic activity in an alkaline medium (1 M KOH). The findings of this research are expected to provide a deeper understanding of the interplay between deposition current density and nanoparticle distribution toward achieving optimal electrode performance in energy systems.

2. Experimental

2.1. Sol Preparation

In this study, cerium chloride ($CeCl_3.7H_2O$) was employed as the cerium source, and hexamethylenetetramine (HMTA) served as the precipitating agent. All reagents were of

[DOI: 10.22068/ijmse.4640]

analytical grade. The use of HMTA yields nanoparticles with a positive surface charge, which enhances the sol-enhanced nanocomposite electrodeposition process. Furthermore, HMTA acts as a complexing precipitating agent that gradually releases OH^- ions, leading to the formation of nanoparticles with a uniform size distribution.

To prepare the sol containing cerium oxide nanoparticles, 0.01 mol (3.73 g) of cerium chloride was dissolved in 100 mL of deionized distilled (DD) water. Subsequently, 0.01 mol (1.42 g) of HMTA, as the precipitating agent, was added to the cerium chloride solution under magnetic stirring. The solution was then heated to 70 °C using a temperature-controlled water bath with a temperature tolerance of ±1 °C, and the sol preparation process was maintained at this temperature under vigorous stirring for 24 hours. A watch glass was placed over the vessel to minimize water evaporation during the prolonged heating period. At the end of the process, the solution volume was restored to 100 mL using deionized distilled water. After 24 hours, the pH of the sol was measured. Upon confirming the absence of residual free hydroxide species released by HMTA (i.e., the solution pH was in the neutral range), the prepared sol was utilized for nanocomposite electrodeposition.

2.2. Nanocomposite Electrodeposition

For the sol-enhanced nanocomposite electrodeposition, the prepared sol containing cerium oxide particles was employed as the nanoparticle source, while a Watts-type bath served as the source of the metallic matrix (cobalt and nickel) in the nanocomposite. The ratio of cobalt to nickel salts in the Watts bath was selected such that the resulting coating would contain 50 wt% of each metallic component within the matrix network. The chemical composition of the Watts bath, the sol-to-electrolyte volume ratio, and the electrodeposition parameters are presented in Table 1. For comparative purposes, a control particle-free alloy coating was deposited at the i_{dep} of 30 $mA.cm^{-2}$.

Electrodeposition was carried out in a standard two-electrode electrochemical cell comprising a cathode (substrate) and an anode (pure nickel sheet). The interelectrode distance was maintained at ~3 cm, and a direct current power supply with a precision of 5 $mA.V^{-1}$ was used for coating deposition. After initial mixing, the electrolyte containing the sol was stirred using a magnetic stirrer for one hour to ensure homogenization and to achieve sufficient surface charging of the particles.

[DOI: 10.22068/ijmse.4640]

Table 1. Electrolyte chemical composition and process parameters for sol-enhanced Ni-Co-CeO_2 electrodeposition

Chemical Composition of the Electrolyte		Electroplating Process Parameters	
Cobalt Sulphate	20 $g.L^{-1}$	Current Density (i_{dep})	10, 20, 30 $mA.cm^{-2}$
Cobalt Chloride	2 $g.L^{-1}$	Current Mode	DC
Nickel Sulphate	160 $g.L^{-1}$	Temperature	Ambient
Nickel Chloride	8 $g.L^{-1}$	Electric Charge	600 C
Boric Acid	20 $g.L^{-1}$	Stirring Speed	400 rpm
Sol-to-Electrolyte	30 vol%		

The cathode substrate was a pure copper sheet. Specimens measuring 1.5 cm × 1.5 cm were cut from the original sheet, and the surface to be coated was ground with up to 1200-grit SiC paper. The lateral surfaces of each specimen were covered with heat-shrinkable plastic insulation to ensure deposition occurred only on one face. Before the deposition, degreasing was performed in a 1 M NaOH solution for one minute, followed by rinsing. Subsequently, surface activation was conducted in a 1 M HCl solution for one minute. After a second rinsing step, electrodeposition was carried out.

2.3. Characterization

Characterization of the prepared cerium oxide sol included scanning electron microscopy (SEM, TESCAN VEGA/XMU, Czech Republic) imaging of dried oxide particles extracted from the sol, as well as particle size analysis of the resulting colloidal sol using dynamic light scattering (DLS - NANO-flex® 180º, Particle Metrix, Germany).

Characterization of the coatings included scanning electron microscopy (SEM, TESCAN VEGA/XMU, Czech Republic) imaging of both the surface and polished cross-sections, elemental composition analysis via energy-dispersive X-ray spectroscopy (EDS), and phase analysis using X-ray diffraction (XRD, Bruker, D8, Germany) on all samples. For EDS analysis, measurements were conducted at three different areas on the surface of each sample, and the average elemental compositions were reported. The incorporation of CeO_2 nanoparticles was evaluated based on the Ce content of the coatings. The phase analysis results were further evaluated using X′Pert HighScore software (Version 3.0). To prepare the fractured cross-sections, the specimens were subjected to a three-point bending test (ASTM B571-91). The wall of cracks generated on the surfaces was considered as the fractured cross-sections [41, 42].

[DOI: 10.22068/ijmse.4640]

2.4. Electrochemical Analysis

Electrochemical measurements were conducted at ambient temperature using an EG&G three-electrode flat cell comprising a working electrode (sample), a reference electrode (Ag/AgCl), and a counter electrode (platinum wire), connected to a computer-controlled galvanostat/potentiostat (FRA - RadStat200) in a 1 M KOH alkaline solution. The exposed surface area of the working electrode in all electrochemical tests was 0.39 cm^2 (corresponding to an orifice diameter of 7 mm). Cyclic voltammetry (CV) was performed within the potential range of 0-0.5 V vs. Ag/AgCl at a scan rate of 1 $mV.s^{-1}$. CV measurements were carried out for three consecutive cycles for each sample, and the most representative response was reported. Electrochemical impedance spectroscopy (EIS) was conducted over a frequency range from 100 kHz to 100 mHz with an amplitude of 5 mV at the open circuit potential of each sample. Galvanostatic charge-discharge (GCD) tests were performed within the potential range of 0-0.35 V at a constant current density (j_{GCD}) of 0.1 $mA.cm^{-2}$. GCD measurements were repeated three consecutive times for each sample, and the best response was reported.

3. Results and Discussion

3.1. Sol Characterization

Figure 1a presents the SE-SEM image of cerium oxide particles extracted from the prepared sol. The micrograph reveals the formation of particles exhibiting spherical and semi-polyhedral morphologies, which tend to form agglomerates due to their high surface energy at the nanoscale. Despite the presence of such agglomerates in the dry state, the granular structure and interparticle porosity remain evident in the image, potentially contributing significantly to the enhancement of the active surface area and the improvement of the electrochemical performance of the final composite coatings.

Furthermore, the stability and size characteristics of these particles in the colloidal phase were assessed via dynamic light scattering (DLS) analysis, as illustrated in Figure 1b. The results indicate that the particles within the sol possess a monomodal and uniform size distribution. According to the corresponding histogram, the mean hydrodynamic diameter of the particles ranges from 200 to 400 nm (with an average particle size of 290 nm), which is in good agreement with the dimensions of the primary particles observed in Figure 1a. The narrow width of the particle size distribution suggests that the sol synthesis method employing

[DOI: 10.22068/ijmse.4640]

hexamine (HMTA) as a precipitating agent effectively prevented uncontrolled particle aggregation, thereby providing a stable suspension of cerium oxide suitable for subsequent electrodeposition processes [43].

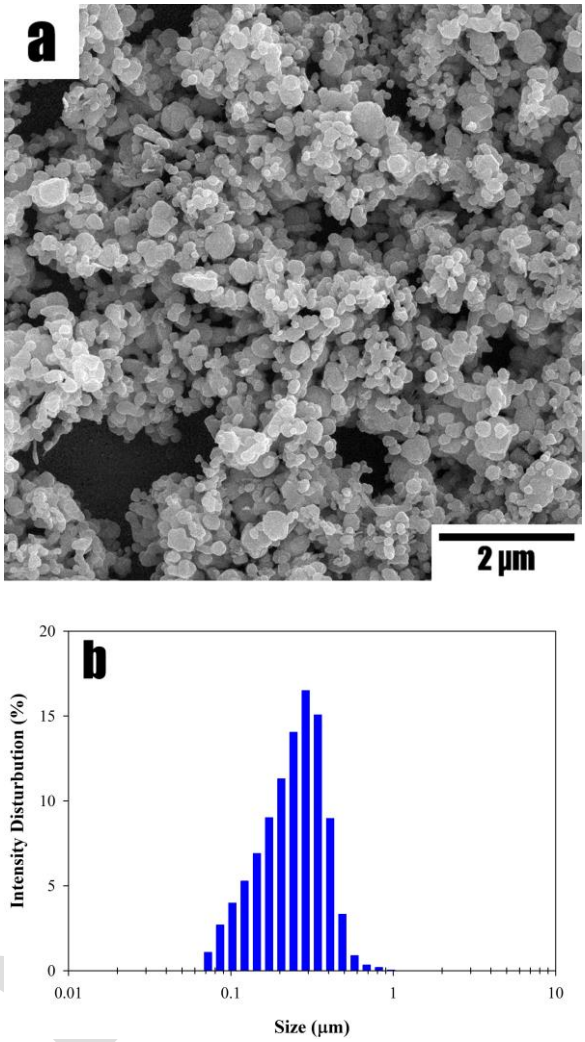

Figure 1. a) SE-SEM image of cerium oxide nanoparticles extracted from the prepared sol, and **b)** size distribution of cerium oxide nanoparticles in the prepared sol, as determined by dynamic light scattering (DLS) analysis

3.2. Coatings Characterization

According to the SEM images presented in Figure 2, the surface morphology and cross-sectional views of the deposited coatings reveal significant structural transformations resulting from the addition of the nanoparticle-containing sol to the electroplating electrolyte and variations in i_{dep}. In the alloy coating prepared without sol addition (Figure 2a), the surface morphology exhibits well-oriented, elongated polyhedral particles arranged in an orderly fashion. Upon incorporation of the CeO_2 nanoparticle sol at different i_{dep} (Figures 2b-2d), this

[DOI: 10.22068/ijmse.4640]

structure undergoes a complete transformation into nanoparticle-containing surfaces with different matrix morphology. The particles precipitated from the sol are clearly distinguishable on the coating surface. However, their surface content diminishes with increasing i_{dep}. Investigation of the influence of i_{dep} on the nanocomposite structures indicates that increasing the i_{dep} from 10 to 30 mA.cm^{-2} alters the particle deposition rate, leading to the formation of denser structures in certain regions. At the lowest i_{dep} (Figure 2b), the cerium oxide particles exhibit a greater tendency to aggregate into large, uniform colloidal clusters with an average size of 3.1±1.0 μm, owing to the sufficient time available for their transport to the electrode surface. However, as illustrated in Figures 2c and 2d, raising the i_{dep} modifies the distribution of these particles, and the surface morphology evolves from a fine granular state toward the formation of larger spherical agglomerates (increasing from 3.3±0.3 μm at i_{dep} of 20 mA.cm^{-2} to 3.7±0.6 μm at i_{dep} of 30 mA.cm^{-2}). It should be noted that the micrometer-scale clusters observed on the coating surface should not necessarily be interpreted as the characteristic size of the incorporated CeO_2 nanoparticles. These features may partly result from localized surface accumulation of nanoparticles during the deposition process, while the nanoparticles incorporated into the coating matrix are expected to be predominantly distributed at the nanoscale.

The fracture cross-sectional images demonstrate the formation of relatively uniform coatings, although the growth mode changes with increasing i_{dep}. In the alloy coating prepared without sol addition (Figure 2-a3), a columnar growth morphology is observed, which is characteristic of electrodeposited coatings [35]. However, upon addition of the sol to the electrolyte, the incorporation of CeO_2 nanoparticles significantly alters the coating growth mode. At the i_{dep} of 10 mA.cm^{-2} (Figure 2-b3), the coating exhibits distinct layers growing approximately parallel to the coating/substrate interface, with CeO_2 nanoparticle incorporation suggested at the interfaces between these layers. With increasing the i_{dep} to 20 mA.cm^{-2} (Figure 2-c3), the growth mode changes considerably, with the columnar structure being replaced by a more randomly oriented grain structure and no apparent evidence of continuous columnar growth. This change can be attributed to the incorporation of CeO_2 nanoparticles, which can interrupt the preferential growth of metallic grains and promote grain refinement [33-35]. Further increasing the i_{dep} to 30 mA.cm^{-2} results in a mixed growth mode, characterized by the coexistence of columnar and randomly oriented regions throughout the coating. These observations indicate that both the presence of CeO_2 nanoparticles and the applied i_{dep} play

[DOI: 10.22068/ijmse.4640]

important roles in controlling the growth mode and microstructural evolution of the deposited coatings.

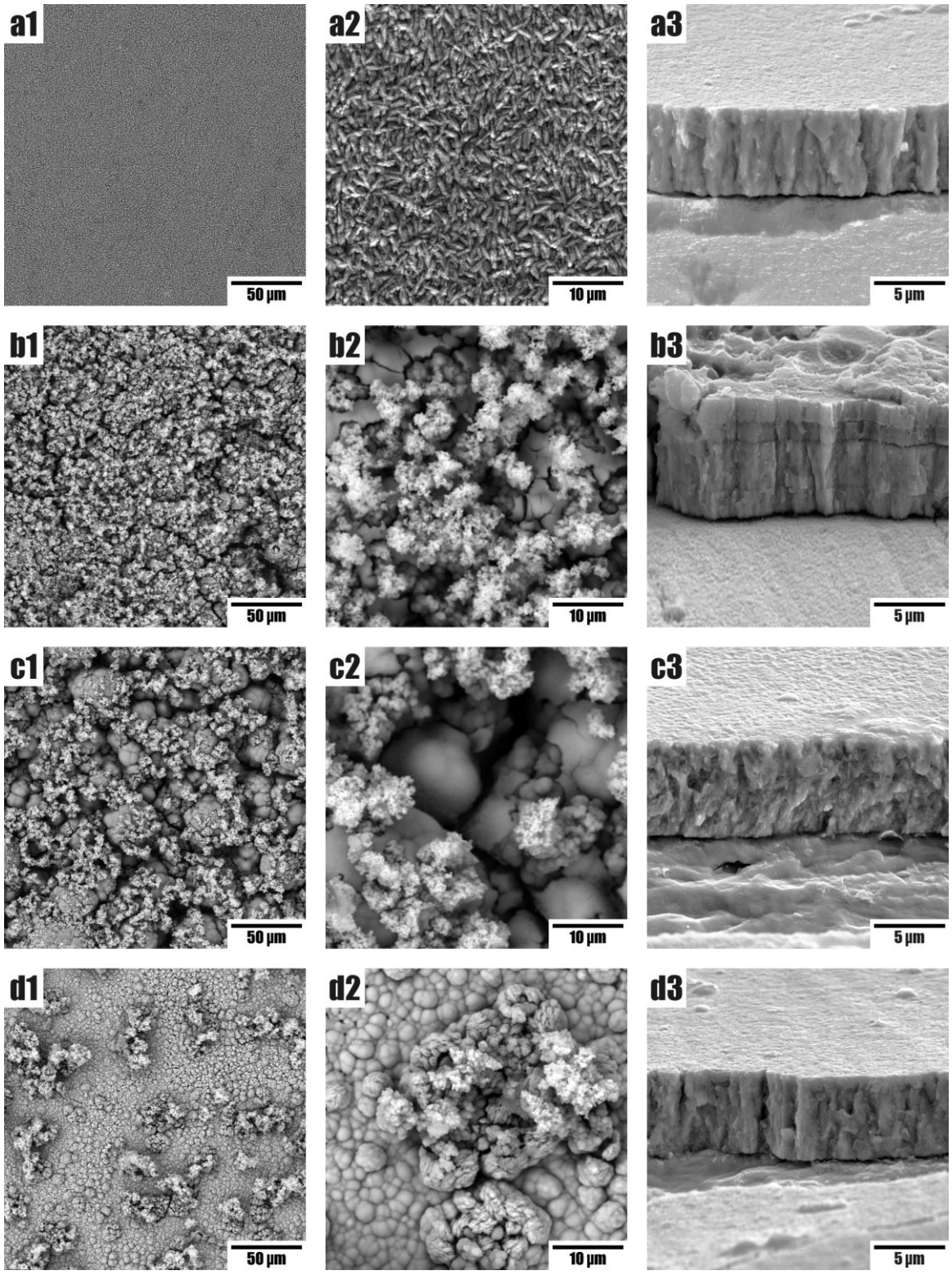

Figure 2. Surface morphology (SE-SEM parts 1 and 2) and fractured cross-section (SE-SEM, part 3) of **a)** particle-free Ni-Co and **b-d)** Ni-Co-CeO_2 nanocomposite coatings electrodeposited at i_{dep} of **b)** 10, **c)** 20, and **d)** 30 $mA.cm^{-2}$

[DOI: 10.22068/ijmse.4640]

It is noteworthy that, despite the micrometer-scale clusters locally observed on the coating surface, no comparable large agglomerates are apparent in the fracture cross-sections. The individual CeO_2 nanoparticles are also beyond the direct resolution of conventional SEM. Nevertheless, the observed microstructural features are consistent with their incorporation and nanoscale dispersion within the metallic matrix. Therefore, the surface clusters should not necessarily be considered representative of the overall nanoparticle distribution throughout the coating.

These structural changes directly affect the surface heterogeneity and the electrochemically active surface area of the coating. Under optimal i_{dep} conditions (20-30 $mA.cm^{-2}$), a balance is established between the deposition rate of metal ions and the entrapment of nanoparticles, resulting in the formation of a three-dimensional architecture featuring controlled surface heterogeneity and adequate mechanical stability in the cross-section.

Figure 3 presents the compositional variations of the nanocomposite coating as a function of applied i_{dep}. The plot demonstrates a direct dependence of the co-deposition behavior of the constituents on the applied i_{dep}. As the i_{dep} increases from 10 to 30 $mA.cm^{-2}$, the weight percentages of cobalt and nickel exhibit a mild upward trend. Specifically, the cobalt content rises from 47.4% to 49.4%, while the nickel content increases from 40.4% to 43.5%. This behavior suggests the predominance of an activation-controlled mass transfer mechanism for the metal ions within this i_{dep} range [8]. The Ni/Co ratio also increases from 0.85 to 0.88 with higher i_{dep}, suggesting the more deposition of Ni in a higher i_{dep}. Conversely, the cerium (Ce) content displays a declining trend with increasing i_{dep}, decreasing from 12.2% at 10 $mA.cm^{-2}$ to 7.1% at 30 $mA.cm^{-2}$. This phenomenon can be attributed to the reduced time available for the diffusion and physical entrapment of cerium oxide particles within the metallic matrix. At higher i_{dep}, the deposition rate of nickel and cobalt ions surpasses the incorporation rate of the insoluble particles, effectively diluting the concentration of nanoparticles in the double-layer adjacent to the electrode surface and, consequently, within the final coating structure. Accordingly, a lower i_{dep} is identified in this study as the parameter enabling the maximum cerium oxide content to be achieved within the nanocomposite structure.

The X-ray diffraction (XRD) patterns corresponding to the deposited coatings, presented in Figure 4, reveal the influence of the incorporation of cerium oxide nanoparticles and variations in i_{dep} on the crystalline structure of the nickel-cobalt matrix. For a better qualitative comparison, the intensity axis of all patterns is normalized to the maximum intensity (I/I_{max}).

[DOI: 10.22068/ijmse.4640]

In the particle-free sample (Figure 4a), the characteristic peaks of the metallic matrix exhibit relatively high intensity and limited broadening, indicating a highly crystalline structure. This sample predominantly exhibits an HCP crystal structure, suggesting the dominant influence of Co in determining the final crystal structure of the electrodeposited layer. Upon incorporation of cerium oxide nanoparticles into the metallic matrix, characteristic peaks corresponding to CeO_2 emerge, while the main metallic peaks undergo pronounced broadening. Furthermore, a peak corresponding to FCC Ni is also detectable in the nanocomposite layers.

The pronounced broadening of the metallic diffraction peaks in the presence of CeO_2 nanoparticles indicates a significant reduction in crystallite size and grain refinement. The calculated crystallite sizes from the main metallic peaks and Scherrer equation [44] were approximately 39, 19, 18, and 25 nm for the particle-free, and sol-enhanced nanocomposite coatings deposited at the i_{dep} of 10, 20, and 30 $mA.cm^{-2}$, respectively. The reduction from 39 nm in the particle-free coating to 19-25 nm in the nanocomposite coatings confirms the grain-refining effect of CeO_2 incorporation. This behavior can be attributed to the ability of the incorporated CeO_2 nanoparticles to act as heterogeneous nucleation sites during electrodeposition, increasing the number of available sites for metallic nucleation and thereby limiting the growth of individual grains. In addition, the nanoparticles can inhibit grain-boundary movement and grain growth through a particle-pinning effect, restricting the coalescence and growth of neighboring crystallites [33]. Therefore, the presence of well-dispersed CeO_2 nanoparticles provides an effective barrier to grain growth and promotes the formation of a finer crystalline structure. The minimum crystallite size of 18 nm obtained at 20 $mA.cm^{-2}$ suggests that this i_{dep} provides the most favorable balance between nanoparticle incorporation and metallic deposition for effective grain refinement.

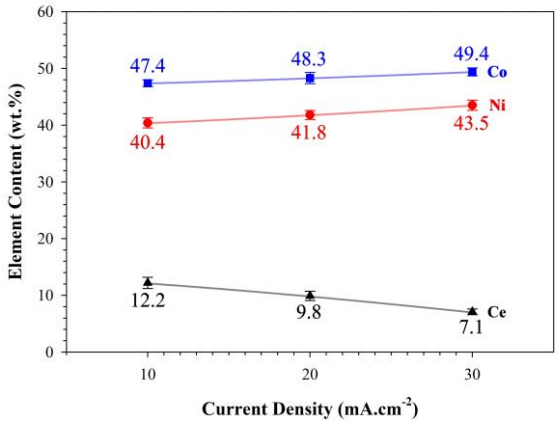

Figure 3. Compositional variations of the nanocomposite coatings as a function of applied i_{dep}, deposited from an electroplating electrolyte containing 30 vol% of the prepared sol

[DOI: 10.22068/ijmse.4640]

An examination of the peak intensity ratio of CeO_2 to the main cobalt peak reveals that this ratio decreases as the i_{dep} increases from 10 to 30 mA.cm^{-2} (from curve b to d in Figure 4). This observation is in agreement with the elemental analysis results; at the lowest i_{dep} of 10 mA.cm^{-2}, a greater opportunity exists for the co-deposition of CeO_2 nanoparticles, resulting in a higher phase fraction within the coating relative to the metallic matrix. Conversely, with increasing i_{dep} and the resulting rise in nickel and cobalt deposition rates, the metallic phase becomes more dominant, and the relative intensity of the CeO_2 peaks in the diffraction pattern diminishes. The increase in crystallite size from 18 nm at i_{dep} of 20 mA.cm^{-2} to 25 nm at i_{dep} ot 30 mA.cm^{-2} may therefore be associated with the reduced incorporation of CeO_2 nanoparticles at higher i_{dep}, which decreases their grain-growth-inhibiting effect.

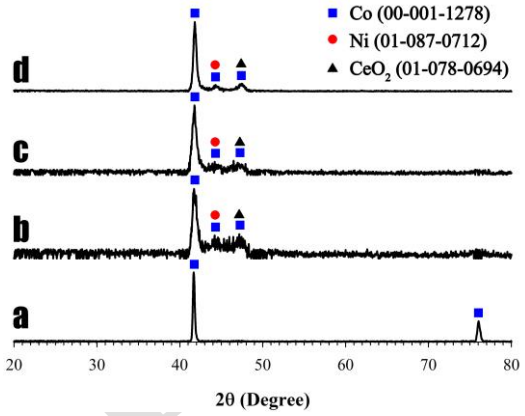

Figure 4. X-Ray diffraction patterns of **a)** particle-free Ni-Co and **b-d)** Ni-Co-CeO_2 nanocomposite coatings electrodeposited at i_{dep} of **b)** 10, **c)** 20, and **d)** 30 mA.cm^{-2}

From the evaluation of the coatings, it can be inferred that the sol-enhanced nanocomposite approach induces significant alterations in the morphology, composition, and crystalline structure of the coating. Microscopic images confirmed that the incorporation of CeO_2 transforms the acicular (needle-like) structure of the nickel-cobalt matrix into a unique architecture featuring controlled surface heterogeneity, wherein i_{dep} plays a decisive role in the compactness of these clusters. Furthermore, in accordance with the elemental analysis data and X-ray diffraction patterns, the i_{dep} of 10 mA.cm^{-2} provides the maximum Ce incorporation (12.2 wt. %), whereas the finest crystallite structure is obtained at i_{dep} of 20 mA.cm^{-2}. This distinction indicates that the amount of incorporated CeO_2 alone does not exclusively determine the final crystallite size; rather, the crystallite refinement is also governed by the deposition kinetics and the interaction between nanoparticle incorporation and metallic grain growth [35]. Hence, the observed reduction in crystallite size in the presence of CeO_2 nanoparticles demonstrates their

[DOI: 10.22068/ijmse.4640]

effective role in suppressing grain growth and promoting a finer crystalline structure, which can provide a favorable microstructural basis for improving the electrochemical performance of the nanocomposite coatings.

3.3. Electrochemical Performance

Evaluation of the electrochemical behavior of the deposited coatings in 1 M KOH alkaline solution using cyclic voltammetry (CV) is presented in Figure 5. The resulting curves display distinct anodic and cathodic peak pairs associated with charge transfer processes within the nickel-cobalt matrix. Comparing the particle-free alloy coating (black line) with the nanocomposite samples reveals that the presence of cerium oxide nanoparticles not only substantially increases the integrated area under the curves for the optimal samples, thereby enhancing the electrochemically active surface area (ECSA), but also alters the nature of the current peaks [15]. The augmented pseudocapacitance observed is a direct consequence of grain refinement and heterogeneity formation induced by the incorporation of cerium oxide nanoparticles, which facilitate electrolyte ion accessibility to internal active sites [24, 29].

A significant observation in the nanocomposite CV curves, particularly at i_{dep} of 20 and 30 $mA.cm^{-2}$ (blue and green lines), is the resolution and splitting of the oxidation peaks. Whereas the particle-free alloy sample exhibits convoluted overlapping peaks for cobalt/nickel oxidation, the presence of cerium oxide yields distinctly separated peaks. This phenomenon is attributed to the catalytic role of cerium oxide in modifying the kinetics of the stepwise reactions of cobalt and nickel [24]. By providing active oxygenated species at the surface, cerium oxide shifts the oxidation potentials of different stages (e.g., transformation of $Ce^{2+} \leftrightarrow Ce^{3+} \leftrightarrow Ce^{4+}$) and resolves the energy levels of these reactions, leading to discrete peaks [29]. This separation indicates the generation of surface sites with differing chemical activities, each responding at a specific potential.

Furthermore, the displacement of anodic peaks toward lower potentials and cathodic peaks toward higher potentials, resulting in a marked reduction in peak potential separation (ΔE_p) to approximately 0.148 V for the optimal sample, indicates decreased polarization and improved reversibility in the presence of nanoparticles. At the optimal deposition i_{dep} (20 $mA.cm^{-2}$), the $j_{CV(anodic)}$ peak increases to 5.8 $mA.cm^{-2}$, confirming enhanced ECSA and increased available charge-transfer sites. A key feature of this sample (blue curve) is the splitting of the main oxidation peak into two distinct peaks at 0.265 V and 0.321 V, reflecting the alteration of the

[DOI: 10.22068/ijmse.4640]

chemical environment around cobalt atoms by cerium oxide nanoparticles. This facilitates the oxidation process at lower overpotentials. Additionally, the steep rise in $j_{CV(anodic)}$ beyond 0.4 V in nanocomposite samples confirms high activity toward the oxygen evolution reaction (OER) [45].

Although at the lowest i_{dep} (10 mA.cm^{-2}), the $j_{CV(anodic)}$peak drops to 2.2 mA.cm^{-2}, potentially due to non-uniform particle aggregation, adjusting the i_{dep} to 20 or 30 mA.cm^{-2} maximizes the synergistic effect between cerium oxide and cobalt/nickel matrix. These results demonstrate that coatings electrodeposited via the sol-enhanced method, owing to uniform nanoparticle distribution and resolved active sites, exhibit substantially higher catalytic stability and efficiency than conventional alloy coatings.

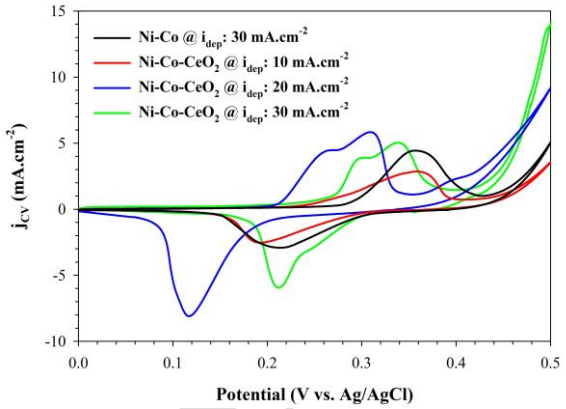

Figure 5. Cyclic voltammetry (CV) curves of particle-free Ni-Co and Ni-Co-CeO_2 nanocomposite coatings recorded at a scan rate of 1 mV.s^{-1} in the potential range of 0 to 0.5 V vs. Ag/AgCl in a 1 M KOH alkaline solution

Electrochemical impedance spectroscopy (EIS) analysis, presented in Figure 6, reveals a close correlation between the chemical composition of the coatings and charge transfer kinetics. Fitting these spectra with elemental analysis data shows that the sample deposited at the i_{dep} of 10 mA.cm^{-2} (red curve), containing the highest cerium oxide content, exhibits the largest Nyquist semicircle and the highest total impedance. This behavior results directly from the semiconducting nature of cerium oxide. The extensive presence of cerium oxide nanoparticles as a high-resistance ceramic phase within the metallic matrix forms a barrier to electron flow, thereby substantially increasing the charge transfer resistance by reducing electrical permeability [12].

As the i_{dep} increases to 20 and 30 mA.cm^{-2}, corresponding to decrease cerium oxide incorporation and tuning the microstructure of the coatings, the diameter of the Nyquist

[DOI: 10.22068/ijmse.4640]

semicircle continuously diminishes. This reduction in impedance arises from the dominance of the conductive metallic phase and the optimized distribution of semiconducting particles within the matrix [32]. In essence, at lower cerium oxide concentrations, the semiconducting properties of the oxide, which at high loadings behave as a relative insulating layer, become moderated, establishing a balance between the catalytically active cerium sites and the high conductivity of the cobalt/nickel matrix.

In the Bode plots (Figures 6b and 6c), the shift in phase angle peaks and the decrease in |Z| at low frequencies for the 30 $mA.cm^{-2}$ sample (green diamonds) confirm the facilitated reaction kinetics resulting from the reduced semiconducting phase fraction. At higher i_{dep}, cerium oxide appears to act not as a resistive barrier but rather as dispersed nucleation centers. By refining the matrix grain structure and providing oxygen-exchange sites (Ce^{3+}/Ce^{4+}) without obstructing conductive pathways, it enhances the overall electrochemical efficiency. This dual behavior implies the critical role of cerium oxide incorporation in determining the ultimate coating performance, transitioning the oxide from a semiconducting insulator to an active electrocatalyst.

Electrochemical impedance spectroscopy (EIS) analysis establishes a direct correlation between quantitative parameters extracted from the equivalent circuit (proposed in Figure 6d) and variations in coating chemical composition induced by changes in i_{dep}, which is presented in Table 2. Examination of the bulk resistance (R_b) values in Table 2 reveals that the sample deposited at 10 $mA.cm^{-2}$, exhibiting a value of 11024 $\Omega.cm^{-2}$, generates the highest resistive barrier to charge transfer. This impedance rise originates from the maximum content of cerium oxide nanoparticles, which form a resistive network within the metallic matrix and restrict electron tunneling pathways owing to their semiconducting and dielectric properties. As the i_{dep} increases to 20 and 30 $mA.cm^{-2}$, the gradual reduction in the weight percentage of this semiconducting phase results in a sharp decline in R_b, reaching 2216 $\Omega.cm^{-2}$ for the 30 $mA.cm^{-2}$ sample. This trend reflects the facilitated reaction kinetics due to the dominance of the conductive Ni-Co phase.

Regarding the capacitive parameters, the increase in CPE_p-T values across all nanocomposite samples relative to the particle-free alloy coating confirms the enhancement of electrochemically active surface area in the presence of nanoparticles [35]. These particles induce micro(nano)-scale roughness and a unique morphology, thereby increasing the effective area in contact with the electrolyte, a trend clearly reflected in the reduction of the heterogeneity

[DOI: 10.22068/ijmse.4640]

exponent (P). Significantly, the lowest P values are recorded at the i_{dep} of 30 mA.cm^{-2} (0.67 for the inner layer and 0.79 for surface porosity), indicating the greatest deviation from ideal capacitive behavior and the formation of a highly porous and rough surface. These CPE variations arise from the interplay between the double-layer capacitance and the space charge capacitance of the semiconducting nanoparticles, collectively enhancing the current responses observed in voltametric tests [32].

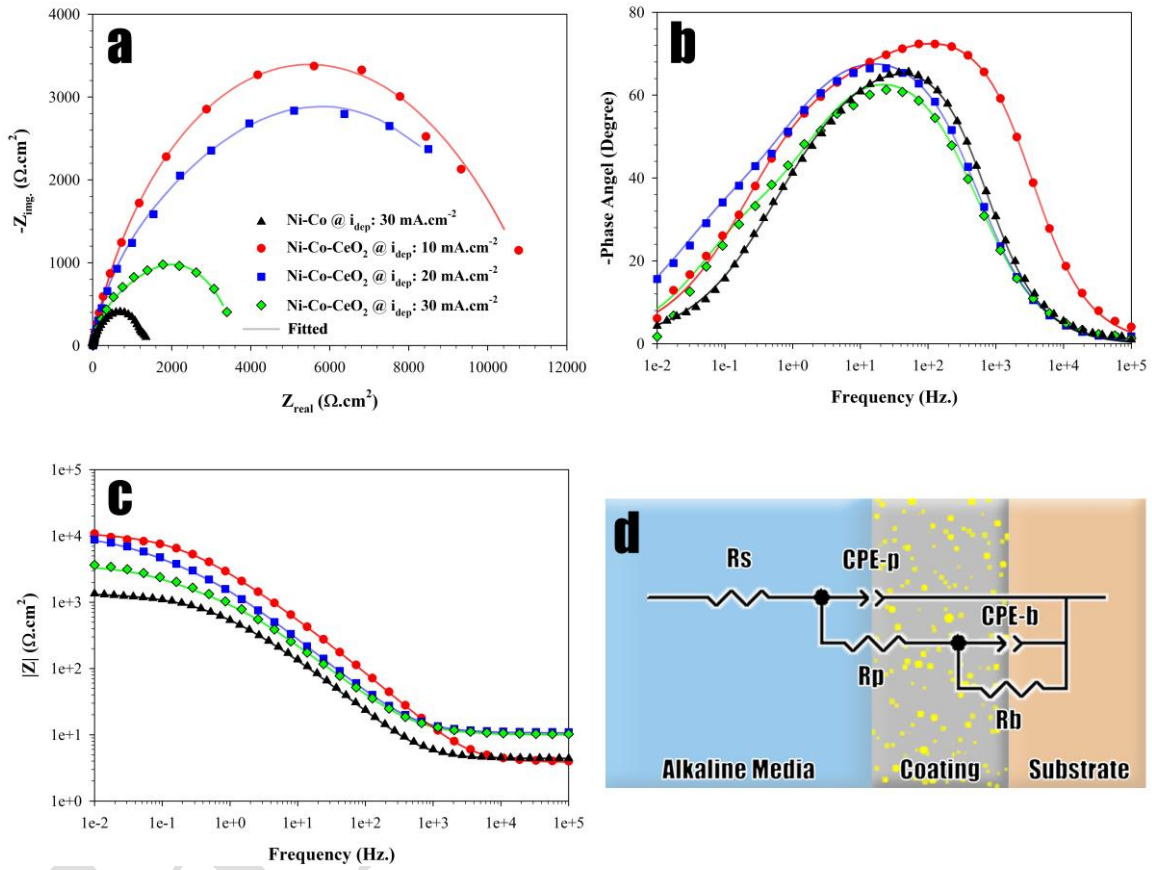

Figure 6. Electrochemical impedance spectroscopy (EIS) analysis curves of particle-free Ni-Co and Ni-Co-CeO_2 nanocomposite coatings obtained in a 1 M KOH alkaline solution: including **a)** Nyquist, **b)** phase angle, **c)** Bode diagrams, and **d)** proposed equivalent circuit

Furthermore, examination of the polarization resistance of the porous layer (R_p) demonstrates that optimizing the i_{dep} not only improves bulk conductivity but also reduces resistance to ion penetration through surface voids. The increase in solution resistance (R_s) from 4.5 Ω.cm^{-2} in the control sample to approximately 10 Ω.cm^{-2} in the nanocomposite samples may be attributed to the increased complexity of ion diffusion pathways due to cerium-induced porosity, which forms a thicker diffusion layer adjacent to the electrode. Ultimately, the equivalent circuit analysis with two-time constants confirms that precise control of the deposition i_{dep} enables an

[DOI: 10.22068/ijmse.4640]

optimal balance between the high catalytic activity derived from Ce^{3+}/Ce^{4+} active centers and the high conductivity of the metallic matrix, yielding minimal charge transfer resistance alongside the maximum available active surface area.

The galvanostatic charge-discharge (GCD) analysis presented in Figure 7, confirms the nonlinear, pseudocapacitive nature of the electrodes at positive potentials, which is fully consistent with the cyclic voltammetry results. Examination of the discharge times reveals that the nanocomposite sample electrodeposited at the i_{dep} of 20 $mA.cm^{-2}$ (blue curve) exhibits the longest discharge duration (~92 seconds), corresponding to the highest charge storage capacity. This performance enhancement, compared with the particle-free alloy coating (black curve: discharge time ~52 seconds), demonstrates the critical role of cerium oxide nanoparticles in increasing the number of active sites for redox reactions and improving the charge retention capability of the coating structure [45].

Table 2. EIS parameters obtained by fitting equivalent circuits for particle-free Ni-Co and Ni-Co-CeO_2 nanocomposite coatings

Sample	Rs ($\Omega.cm^2$)	CPE_p-T ($S.s^p.cm^{-2}$)	CPE_p-P	Rp ($\Omega.cm^2$)	CPE_b-T ($S.s^p.cm^{-2}$)	CPE_b-P	Rb ($\Omega.cm^2$)
Ni-Co i:20	4.5	7.7×10^{-5}	0.94	2	3.5×10^{-4}	0.58	1404
Ni-Co-CeO_2 i:10	3.9	3.8×10^{-5}	0.89	678	6.6×10^{-5}	0.55	11024
Ni-Co-CeO_2 i:20	10.8	1.2×10^{-4}	0.82	3089	2.7×10^{-4}	0.59	8152
Ni-Co-CeO_2 i:30	10.1	1.6×10^{-4}	0.79	1438	6.7×10^{-4}	0.67	2216

The relative symmetry between the charge and discharge curves in the nanocomposite samples, particularly at 20 and 30 $mA.cm^{-2}$, indicates high coulombic efficiency and favorable electrochemical reversibility. In contrast, the sample fabricated at 10 $mA.cm^{-2}$ (red curve) shows the shortest discharge time, a performance decline consistent with the very high charge transfer resistance recorded for this sample in impedance testing. Indeed, although the high cerium oxide content in this sample increases catalytic active centers, its semiconducting nature induces an initial ohmic (IR) drop at the onset of discharge, thereby reducing charge retention duration.

Analysis of the curve slopes demonstrates that optimizing the i_{dep} to 20 $mA.cm^{-2}$ establishes an ideal balance between the conductivity of the metallic matrix and the catalytic activity of the semiconducting nanoparticles. Consequently, the discharge process proceeds with greater

[DOI: 10.22068/ijmse.4640]

stability, maintaining the potential level over a longer period. The recovery of discharge time in the 30 mA.cm^{-2} sample (green curve) relative to the 10 mA.cm^{-2} sample further supports the conclusion that reducing the semiconducting particle concentration at higher i_{dep} improves current distribution and facilitates charge transfer reactions throughout the coating, rendering these electrodes suitable candidates for energy storage and electrocatalytic applications.

In summary, the electrochemical evaluations conducted on the Ni-Co-CeO_2 nanocomposite coatings reveal a direct and engineered relationship between synthesis parameters and surface catalytic responses. The presence of cerium oxide nanoparticles, by forming a heterogeneous, fine-grained structure, not only significantly enhances the electrochemically active surface area but also provides parallel, facilitated pathways for charge transfer reactions via Ce^{3+}/Ce^{4+} redox couples. This leads to the resolution of metal oxidation peaks and a reduction in the reaction onset potential. Although the semiconducting nature of these nanoparticles at high concentrations (e.g., in the sample deposited at 10 mA.cm^{-2}) results in increased charge transfer resistance, optimizing the i_{dep} to 20 mA.cm^{-2} establishes an effective balance between the conductivity of the metallic matrix and the catalytic activity of the oxide phase. This is evidenced by the longest discharge time in GCD tests and a significant reduction in bulk resistance compared with other composite samples in EIS analysis. Consequently, the role of cerium oxide in this structure extends beyond morphological reinforcement. It acts as an active co-catalyst, improving reaction reversibility and facilitating interfacial electrode/electrolyte kinetics, thereby enhancing the practical performance of the coating in energy-related systems.

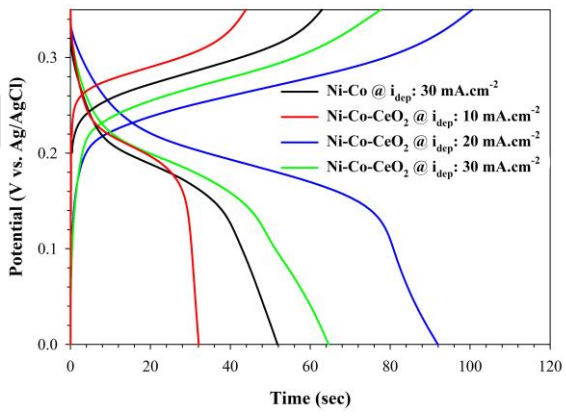

Figure 7. The galvanostatic charge-discharge (GCD) curves of particle-free Ni-Co and Ni-Co-CeO_2 nanocomposite coatings recorded at a j_{GCD} of 0.1 mA.cm^{-2} in the potential range of 0 to 0.35 V vs. Ag/AgCl in a 1 M KOH alkaline solution

[DOI: 10.22068/ijmse.4640]

4. Conclusion

The primary conclusions derived from this research are summarized below:

1- Synthesis of the CeO_2 sol yielded uniform, monomodal nanoparticles with an average hydrodynamic diameter of 290 nm (range: 200-400 nm). Their distinct spherical/semi-polyhedral morphology and porous structures effectively prevent uncontrolled aggregation, successfully providing an enhanced active surface area for superior electrochemical coating performance.

2- Sol-enhanced electrodeposition altered the polyhedral structure of the particle-free alloy coatings into a unique, nanostructured composite. At optimal i_{dep} (20-30 $mA.cm^{-2}$), a balance between metal deposition and nanoparticle entrapment established a uniform, well-adherent 3D architecture with controlled heterogeneity for enhanced active surface area.

3- Increasing i_{dep} (10-30 $mA.cm^{-2}$) triggered activation-controlled deposition, raising nickel (40.4 wt. % - 43.5 wt. %) and cobalt (47.4 wt. % - 49.4 wt. %) contents while increasing the Ni/Co ratio (0.85-0.88). Conversely, mass-transfer limitations reduced the embedded cerium content from 12.2 wt. % to 7.1 wt. %, identifying lower i_{dep} as optimal for maximum nanoparticle incorporation.

4- Incorporating CeO_2 nanoparticles into the HCP Co matrix successfully induced grain refinement, reducing crystallite size via heterogeneous nucleation while introducing FCC Ni phases. Reflecting elemental data, increasing i_{dep} (10-30 $mA.cm^{-2}$) systematically decreased the CeO_2-to-cobalt XRD peak intensity ratio due to dominant metallic phase deposition.

5- Cyclic voltammetry analysis illustrated that incorporating CeO_2 nanoparticles into the Ni-Co matrix enhanced pseudocapacitance, reduced peak separation (ΔE_p) to 0.148 V. at an optimal i_{dep} of 20 $mA.cm^{-2}$, uniform nanoparticle distribution maximized ECSA, boosting $j_{CV(anodic)}$ peak to 5.8 $mA.cm^{-2}$ and splitting the oxidation peak into discrete responses at 0.265 V and 0.321 V, confirming improved reversibility and resolved multi-step reaction kinetics.

6- The equivalent circuit modeling from the EIS study of prepared electrodes demonstrated that increasing i_{dep} (10-30 $mA.cm^{-2}$) systematically lowered bulk resistance (R_b) from 11,024 to 2,216 $\Omega.cm^{-2}$ by minimizing the semiconducting CeO_2 phase. Simultaneously, enhanced surface roughness lowered the heterogeneity exponent (P) to 0.67, maximizing active surface area (CPE_p) and ion penetration while optimizing charge-transfer kinetics.

[DOI: 10.22068/ijmse.4640]

7- GCD profiles of prepared electrodes confirmed the pseudocapacitive nature of the composite coatings. Optimizing the i_{dep} to 20 mA.cm^{-2} maximized active site availability, increasing the discharge duration from 52 (for particle-free alloy electrode) to 92 seconds. This optimization eliminated the initial IR drop observed in the electrode deposited at 10 mA.cm^{-2}, balancing metallic matrix conductivity with nanoparticle catalytic activity for superior electrochemical reversibility.

References

[1] Adeyinka, A. M., Esan, O. C., Ijaola, A. O. and Farayibi, P. K., "*Advancements in hybrid energy storage systems for enhancing renewable energy-to-grid integration.*" Sustain. Energy Res., 2024, 11, 26-26.

[2] Yu, H., Zhang, J., Shaheen, I., Ahmad, M., Chen, X., Akkinepally, B. and Hussain, I., "*Nature-resembled nanostructures for energy storage/conversion applications.*" J. Ind. Eng. Chem., 2024, 129, 53-68.

[3] Venkatesan, S. V., Nandy, A., Karan, K., Larter, S. R., and Thangadurai, V., "*Recent advances in the unconventional design of electrochemical energy storage and conversion devices.*" Electrochem. Energy Rev., 2022, 5, 16.

[4] Li, F., Huang, L., Zaman, S., Guo, W., Liu, H., Guo, X. and Xia, B. Y., "*Corrosion chemistry of electrocatalysts.*" Adv. Mater., 2022, 34, 2200840.

[5] Han, Y., Wang, J., Liu, Y., Li, T., Wang, T., Li, X., Ye, X., Li, G., Li, J., Hu, W. and Deng, Y., "*Stability challenges and opportunities of NiFe-based electrocatalysts for oxygen evolution reaction in alkaline media.*" Carbon Neutralization, 2024, 3, 172-198.

[6] Wang, W. W., Chen, C., Liu, Z. X., Zhu, Q. X., Zu, Y. X., Lu, Z. Q., Zhang, B., Yu, Z. P. and Xu, G. Y., "*From laboratory to industrial scale: nickel-based catalysts for hydrogen evolution under high current-density alkaline electrolysis.*" Rare Met., 2025, 44, 9507-9542.

[7] Derakhshani, M., Rastegari, S. and Ghaffarinejad, A., "*Foam-like electroplated Ni-W/graphene oxide composite coating with high porous surface: an efficient electrocatalyst for the hydrogen evolution reaction.*" Iran. J. Mater. Sci. Eng., 2025, 22, 129-136.

[DOI: 10.22068/ijmse.4640]

[8] Derakhshani, M., Rastegari, S. and Ghaffarinejad, A., "*Ni-W alloy coating as an efficient electrocatalyst for the hydrogen evolution reaction: effect of electroplating current density on morphology and electrocatalytic properties.*" Iran. J. Mater. Sci. Eng., 2024, 21, 45-52.

[9] Do, V. and Lee, J., "*Surface engineering for stable electrocatalysis.*" Chem. Soc. Rev., 2024, 53, 2693-2737.

[10] Yao, Q., Yu, Z., Li, L. and Huang, X., "*Strain and surface engineering of multicomponent metallic nanomaterials with unconventional phases.*" Chem. Rev., 2023, 123, 9676-9717.

[11] Pazhamalai, P., Krishnan, V., Saleem, M. S. M., Kim, S. K. and Seo, H. W., "*Investigating composite electrode materials of metal oxides for advanced energy storage applications.*" Nano Converg., 2024, 11, 30-30.

[12] Sabze Var, F., Sarraf, S., Rastegari, S. and Soltanieh, M., "*Response surface methodology optimization of electroplating parameters for Co/CeO_2 composite coatings with enhanced corrosion and wear resistance.*" J. Mater. Res. Technol., 2025, 38, 4049-4063.

[13] Chen, Y., Yang, H., Feng, H., Yang, P., Zhang, J. and Shu, B., "*Electrodeposition and corrosion performance of Ni-Co alloys with different cobalt contents.*" Mater. Today Commun., 2023, 35, 106058-106058.

[14] Radadi, R. M. A. and Ibrahim, M. A. M., "*Nickel-cobalt alloy coatings prepared by electrodeposition Part II: Morphology, structure, microhardness, and electrochemical studies.*" Korean J. Chem. Eng., 2021, 38, 152-162.

[15] Khoshkalam, A. A., Sarraf, S. and Rastegari, S., "*Tailoring porous Ni–Co alloy structures via dynamic hydrogen bubble templating (DHBT) using a design of experiments approach.*" J. Mater. Res. Technol., 2026, 43, 6682-6695.

[16] Abdel-Karim, R., Ramadan, M. and El-Raghy, S. M., "*Morphology and electrochemical characterization of electrodeposited nanocrystalline Ni-Co electrodes for methanol fuel cells.*" J. Nanomater., 2018, 2018, 9870732.

[17] Xiao, M. and Sun, H., "*Preparation of nickel and cobalt-based micro-nano structural materials and their applications in energy storage and conversion.*" Chem. Rec., 2025, 25, e202500157.

[DOI: 10.22068/ijmse.4640]

[18] Tantawy, N. S., Heakal, F. E. and Ahmed, S. Y., "*Synthesis of worm-like binary metallic active material by electroless deposition approach for high-performance supercapacitor.*" J. Energy Storage, 2020, 31, 101625.

[19] Mohapatra, S., Das, H. T., Tripathy, B. C. and Das, N., "*Recent developments in electrodeposition of transition metal chalcogenides-based electrode materials for advance supercapacitor applications: A review.*" Chem. Rec., 2024, 24, e202300220.

[20] Li, D., Li, Y., Xu, Z., Wang, D., Wang, T., Zhao, J. and Zhang, H., "*Core/shell Ni-P@Ni-Co composite with micro-/nanostructure for supercapacitor.*" J. Mater. Sci., 2018, 53, 3647-3660.

[21] Kumar, K. D., Kumar, Y. A., Ramachandran, T., Al-Kahtani, A. and Kang, M., "*Cactus-like Ni-Co/$CoMn_2O_4$ composites on Ni foam: Unveiling the potential for advanced electrochemical materials for pseudocapacitors.*" Mater. Sci. Eng. B, 2023, 296, 116715.

[22] Kumar, A. and Shah, M. A., "*Superior electrochemical energy storage in Ni/Co/Zr ternary composite: Insights from synthesis to performance in supercapacitors.*" Next Mater., 2025, 8, 100889.

[23] Coviello, D., Contursi, M., Toniolo, R. and Casella, I. G., "*Electrochemical and spectroscopic investigation of a binary Ni-Co oxide active material deposited on graphene/polyvinyl alcohol composite substrate.*" J. Electroanal. Chem., 2017, 791, 117-123.

[24] Phokha, S., Hunpratub, S., Usher, B., Pimsawat, A., Chanlek, N. and Maensiri, S., "*Effects of CeO_2 nanoparticles on electrochemical properties of carbon/CeO_2 composites.*" Appl. Surf. Sci., 2018, 446, 36-46.

[25] Ansari, M. N., Gouadria, S., Khosa, R. Y., Manzoor, S., Abdullah, M., Abid, A. G., Ahmad, N., Aman, S. and Farid, H. M. T., "*Nanospheres type morphology for regulating the electrochemical property of CeO_2 nanostructures for energy storage system.*" J. Sol-Gel Sci. Technol., 2023, 106, 121-130.

[26] Joseph, A., Perikkathra, S. and Thomas, T., "*Novel 2D CeO_2 nanoflakes as a high-performance asymmetric supercapacitor electrode material*." J. Energy Storage, 2023, 68, 107757.

[DOI: 10.22068/ijmse.4640]

[27] Deng, D., Chen, N., Xiao, X., Du, S. and Wang, Y., "*Electrochemical performance of CeO_2 nanoparticle-decorated graphene oxide as an electrode material for supercapacitor.*" Ionics, 2017, 23, 121-129.

[28] Mujtaba, A. and Janjua, N. K., "*Electrochemical sensing platform based on CuO@CeO_2 hybrid oxides.*" J. Electroanal. Chem., 2016, 763, 125-133.

[29] Phokha, S., Hunpratub, S., Chanlek, N., Sonsupap, S. and Maensiri, S., "*Synthesis, characterization and electrochemical performance of carbon/Ni-doped CeO_2 composites.*" J. Alloys Compd., 2018, 750, 788-797.

[30] Sarwar, M., Shahbaz, M., Ghaffar, R., Saleem, M., Khan, M. Z., Irshad, M., Sharif, S., Koh, J. H., Haseeb, M., Ghaffar, A., Shakir, I. and Ali, K., "*Robust cyclic stability and high-power performance of Ni/Mg co-doped CeO_2 electrodes for asymmetric hybrid supercapacitors.*" Mater. Today Sustain., 2026, 33, 101272.

[31] Vanitha, M., Kamble, N. K., Vinayagam, P., Muthukumar, T., Sasikumar, M. S. S. and Kumaran, S., "*Enhancing EDLC-pseudocapacitive performance of flexible CeO_2 electrode via design of Ni-doped CeO_2 nanoparticles grafted @ chitosan biopolymer hybrid framework for supercapacitor applications.*" J. Nanopart. Res., 2026, 28, 85.

[32] Zhang, D., Zheng, S., Yu, L., Chen, L., Chen, J. and Wang, Y., "*Preparation and characterization of the Ni-C composite coating electrodeposited with carbon sol.*" J. Mater. Res. Technol., 2023, 22, 206-215.

[33] Wang, Y., Wang, S., Shu, X., Gao, W., Lu, W. and Yan, B., "*Preparation and property of sol-enhanced Ni-B-TiO_2 nano-composite coatings.*" J. Alloys Compd., 2014, 617, 472-478.

[34] Chen, W. and Gao, W., "*Microstructures and properties of sol-enhanced nanostructured metal-oxide composite coatings.*" Prog. Nat. Sci.: Mater. Int., 2011, 21, 355-362.

[35] Sarraf, S. H., Rastegari, S. and Soltanieh, M., "*Deposition of mono dispersed Co-CeO_2 nanocomposite coatings by a sol-enhanced pulsed reverse electroplating: process parameters screening.*" J. Mater. Res. Technol., 2023, 23, 3772-3789.

[36] Wang, Y., Gao, W., He, Z., Jin, Y., Qiao, Y., Cheng, G., Gao, W. and Zhi, Z., "*Cu-Sn-Zn nanocomposite coatings prepared by TiO_2 sol-enhanced electrodeposition.*" J. Appl. Electrochem., 2020, 50, 875-885.

[DOI: 10.22068/ijmse.4640]

[37] He, Z., Zhou, Y., Wang, Y., Guo, P., Jiang, W., Yao, C. and Shu, X., "*Preparation and properties of Ni-W-P-TiO_2 nanocomposite coatings developed by a sol-enhanced electroplating method.*" Chin. J. Chem. Eng., 2022, 44, 369-376.

[38] Ghaziof, S. and Gao, W., "*Zn-Ni-Al_2O_3 nano-composite coatings prepared by sol-enhanced electroplating.*" Appl. Surf. Sci., 2015, 351, 869-879.

[39] Wang, Y., Cao, D., Gao, W., Qiao, Y., Jin, Y., Cheng, G., Gao, W. and Zhi, Z., "*Microstructure and properties of sol-enhanced Co-P-TiO_2 nano-composite coatings.*" J. Alloys Compd., 2019, 792, 617-625.

[40] Kallel, M., Masseoud, M., Vesco, S., Barletta, M. and Elleuch, K., "*The effects of TiO_2 sol concentration on single- and multiple-scratch damage in electroplated Ni-B-TiO_2 sol composite coating.*" Ceram. Int., 2020, 46, 3767-3776.

[41] Nabavi, R., Sarraf, S. and Soltanieh, M., "*Optimization of hard anodizing process parameters on 6061-T6 aluminum alloy using response surface methodology.*" J. Mater. Eng. Perform., 2024, 33, 10048-10061.

[42] Sabzehvar, F., Sarraf, S., Soltanieh, M. and Seyedein, S. H., "*Improving bioactivity of anodic titanium oxide (ATO) layers with chlorine ion addition in electrolytes.*" Ceram. Int., 2025, 51, 3493-3509.

[43] Parimi, D., Sundararajan, V., Sadak, O., Gunasekaran, S., Mohideen, S. S. and Sundaramurthy, A., "*Synthesis of positively and negatively charged CeO_2 nanoparticles: Investigation of the role of surface charge on growth and development of drosophila melanogaster.*" ACS Omega, 2019, 4, 104-113.

[44] Shahri, Z. and Allahkaram, S. R., "*Effect of particles concentration and current density on the cobalt/hexagonal boron nitride nano-composite coatings properties.*" Iran. J. Mater. Sci. Eng., 2012, 9, 1-7.

[45] Kumar, K., Saranya, P. E. and Rosy, P. J., "*Exploring the mixed morphology of CeO_2 nanorods and nanoparticles for enhanced asymmetric supercapacitor and electrochemical sensor applications.*" Mater. Chem. Phys., 2025, 345, 131259.

[DOI: 10.22068/ijmse.4640]